

Enhancement and Validation of VPM-Derived State-Space Inflow Models for Multi-Rotor Simulation

Matthew Gladfelter, Chengjian He, and Chongseok Chang
Advanced Rotorcraft Technology, Inc.
Sunnyvale, CA 94085, USA

Mark B. Tischler and Mark J.S. Lopez

V_{tip} Rotor tip speed R
 $w_i(r; t)$ i th Rotor inflow over the rotor plane
 w_{intf} Rotor induced interference velocity (off-rotor)
 \bar{w}_{intf} Effective rotor interference velocity on fuselage]TJ/F46 9.962

$$w_i(r; \theta; t) = \sum_{m=0}^{\infty} \sum_{n=m+1; m+3; \dots}^{\infty} m_n(r) [\frac{mci}{n}(t) \cos(m\theta) + \frac{msi}{n}(t) \sin(m\theta)] \quad (1)$$

$$\text{States: } M_i \begin{bmatrix} mci \\ -m \\ nsi \\ -n \end{bmatrix} + L_i^{-1} [V]_i \begin{bmatrix} mci \\ n \\ msi \\ n \end{bmatrix} = \begin{bmatrix} mci(t) \\ n \\ msi(t) \\ n \end{bmatrix} + \frac{K_{rot,i}}{s+1} \begin{bmatrix} q \\ p \end{bmatrix} \quad (2)$$

$$\text{Outputs: } w_{ji}^{intf}(r_j; \theta_j; t) = H_i^j \begin{bmatrix} mci(t) \\ n \\ msi(t) \\ n \end{bmatrix} \quad (3)$$

Unified Inflow Model Formulation

The studies described in this paper continue the use of the multi-rotor inflow formulation used in the previous studies of Ref. [7] and [8]. The finite state inflow model is structured with state and output equations where the state equation governs an individual rotor's inflow dynamics while the output equations formulate the influence of the rotor inflow on other rotors, surfaces, locations, etc. First, the induced inflow distribution equation is presented in the form of Equation 1.

Equation 1 describes the inflow distribution over the i -th rotor of a multi-rotor system. In this equation, $\frac{mci}{n}$ and $\frac{msi}{n}$ are the inflow states of the i -th rotor, $m_n(r)$ is the radial inflow variation shape function, and $w_i(r; \theta; t)$ is the induced inflow distribution described by radial position, azimuthal position, and instance in time.

For the i -th rotor, the inflow dynamics and output formulation is described by Equations 2 and 3,

$$\begin{matrix}
 \begin{matrix} 8 \\ < \\ : \\ \end{matrix} & \begin{matrix} \textcircled{9} \\ \\ ; \\ \end{matrix} & \begin{matrix} 2 \\ \\ \\ \end{matrix} & \begin{matrix} h_{11} & h_{12} & h_{13} \\ h_{21} & h_{22} & h_{23} \\ h_{31} & h_{32} & h_{33} \end{matrix} & \begin{matrix} 3 \\ < \\ : \\ \end{matrix} & \begin{matrix} \textcircled{8} \\ \\ \\ \end{matrix} & \begin{matrix} \begin{pmatrix} 0c1(t) \\ \frac{1}{2}c1(t) \\ \frac{1}{2}s1(t) \end{pmatrix} \\ \\ \\ \end{matrix} & \begin{matrix} \textcircled{9} \\ \\ ; \\ \end{matrix} \\
 & + & \begin{matrix} 4 \\ \\ \\ \end{matrix} & \begin{matrix} h_{11} & h_{12} & h_{13} \\ h_{21} & h_{22} & h_{23} \\ h_{31} & h_{32} & h_{33} \end{matrix} & \begin{matrix} 5 \\ < \\ : \\ \end{matrix} & \begin{matrix} \textcircled{8} \\ \\ \\ \end{matrix} & \begin{matrix} \begin{pmatrix} 0c2(t) \\ \frac{1}{2}c2(t) \\ \frac{1}{2}s2(t) \end{pmatrix} \\ \\ \\ \end{matrix} & \begin{matrix} \textcircled{9} \\ \\ ; \\ \end{matrix} \\
 & & & & & & & (6)
 \end{matrix}$$

This equation structure illustrates the individual parameters that are to be identified to fully capture the interference characteristics for the co-axial rotor configuration. The interference velocity as a vector of directional components allows for ease of implementation into the simulation model.

For the rotor interference on fuselage specifically, an investigation was conducted to determine if an effective interference velocity averaged from a series of sampling points across the fuselage surface could yield a more accurate identified model versus sampling at the c.g. as was done in Ref. [8]. The formulation for this effective interference velocity is

$$w_{intf} = \frac{\sum_{j=1}^N l_j w_{intf,j}}{N} \quad (7)$$

where w_{intf} is the effective velocity averaged from N sample points with the weighting l_j applied. l_j is the nondimensionalized offset factor of point j with respect to the moment center to account for the interference influence on the fuselage moments.

Inflow Model Parameter Identification and Verification

The identification methodology developed in Ref. [7] and enhanced in [8] was applied to a generic co-axial vehicle designed based on the study conducted in Ref. [20]. Figure 1 presents the co-axial vehicle configuration. The identification methodology is outlined in Figure 2 with the critical steps as follows:

A multi-rotor model is created and coupled with VPM inflow. The vehicle fuselage is included so that wake blockage effects are accounted for. The rotor model is run at the flight condition of interest while a 90 second frequency sweep excitation is applied to one rotor through a forcing function. The response of each rotor's inflow states as well as the rotor interference at points of interest are collected during the run. Therefore, mutual interference between rotors is captured for multiple rotor configurations.

CIFER^R is used to determine frequency domain responses from the VPM-generated time histories. From the frequency responses, CIFER^R identifies a finite state inflow model through fitting cost optimization. For the inflow model identification application, an automated tool was developed via the Command Line Interface to conduct the process in batch.

The identified inflow model is verified in both the frequency and time domain to ensure that accurate parameters were obtained. VPM is run as the baseline response to judge accuracy.

The identified inflow model is integrated into a flight simulation model. The current implementation for a FLIGHTLAB simulation model is table lookup. The full vehicle flight dynamic response is then evaluated.

Using this process, an identified inflow model was developed for the co-axial configuration described. A co-axial rotor model was constructed with VPM coupling, and forcing function excitations with characteristics illustrated in Figure 3 were applied to generate inflow state frequency response data. Figure 4 shows the upper rotor inflow state and lower rotor expansion coefficient response for an upper rotor cosine excitation (second excitation shown in Fig 3) generated from the VPM-coupled coaxial rotor model at 40 knots as an example of the frequency response data of interest. CIFER^R was used to construct the identified 3-state inflow model from these time histories. Figure 5TJ 0 -11.956 Td

An important detail of this identification process is that the rotor on rotor mutual interference is determined alongside the individual rotor inflow state parameters. Since both rotors are present when the VPM coupled response data is generated, the same run is used in the identification of $[M]$, $[L]$, and \dot{h}_i in Equation 2 as for $[H]$ and \dot{h}_h in Equation 3. By determining the mutual rotor interactions in this manner, the identification methodology captures a critical multi-rotor phenomenon in a way that naturally progresses from the inflow state identification process.

Rotor TPP Rotation Effect

While the identification process described in the previous section has been proven as a robust method for establishing an accurate base inflow model, an additional term is required to model the distortion effects that occur as caused by the rotor TPP rotation. An additional identification procedure was developed and conducted to obtain values of K_{rot} and \dot{h}_k as formulated in Equation 2. This section details the rotor TPP rotation identification process, verification of the identified parameters, and the resulting impacts on the full vehicle flight dynamics. Emphasis is placed on applications not addressed in Ref. [8] such as integration into a linear flight dynamics model and identification at transitional airspeeds.

Rotor TPP Rotation Identification and Verification

The method used to determine the TPP rotation effect parameters is similar to the inflow model identification process. A VPM-coupled multi-rotor simulation model constructed in FLIGHTLAB is excited with hub frequency sweep rotations of an individual rotor. The same FLIGHTLAB simulation model used in the inflow model identification can be used in TPP rotation effect parameter identification. For the generic co-axial configuration, frequency sweeps of a hub's rotation rate were performed over 90 seconds with an 8 degrees per second amplitude (allowing for the 52r for the parameters of trs

Table 2: Identified K_{rot} factors and time constants for the generic co-axial rotor at 15 knots

Frequency Response	Rotor Excited	K_{rot}	K_r	i	k
$\frac{1}{2}c^1=q$	Upper	0.0055	0.22	0.127	1.8
$\frac{1}{2}c^2=q$	Lower	0.0065	0.24	0.091	1.8
$\frac{1}{2}s^1=p$	Upper	0.0035	0.28	0.172	1.7
$\frac{1}{2}s^2=p$	Lower	0.0033	0.26	0.164	1.5

Table 3: Identified K_{rot} factors and time constants for the generic co-axial rotor at 40 knots

Frequency Response	Rotor Excited	K_{rot}	K_r	i	k
$\frac{1}{2}c^1=q$	Upper	0.0045	0.11	0.024	1.6
$\frac{1}{2}c^2=q$	Lower	0.0084	0.14	0.002	1.8
$\frac{1}{2}s^1=p$	Upper	0.0065	0.18	0.144	1.5
$\frac{1}{2}s^2=p$	Lower	0.0051	0.17	0.196	1.3

Using Equation 4 and L as identified for each

show how inclusion of the TPP rotation identification improves the inflow model. The improvement to the low frequency range is again most notable.

The hover investigation was further expanded beyond Ref. [8] by assessing the inflow model and TPP rotation effect for the application of a linear time-invariant (LTI) model. Because the LTI model is often more appropriate for performance evaluation

are $J = 100$, indicating satisfactory model accuracy (Ref. [13]). Figures 30 and 31 suggest that the impact of interference at the tail on the pitch and roll response is negligible. Because the tail surfaces are outside the main rotor wake for the hover flight condition, this result is expected. For the heave response to collective (Fig. 32) and the yaw rate response to pedal (Fig. 33), inclusion of the rotor interference did improve the low frequency response a small amount, suggesting that the low frequency excitations of these channels influenced the rotor wake enough to impact the tail surface effectiveness at hover. For both cases, however, the fitting cost is acceptable even without the interference model. To further explore the accuracy of the interference model, the aerodynamic surface interference velocities and forces were collected and evaluated for the hover trim condition. Table 5 presents the collected data for the left stabilator surface. The identified interference model corrects the downwash

Table 7: Force and error comparison for various fuselage interference approximation methods, hover

	Single Point (C.G.)	Algebraic Average	Offset Weighted Average	VPM-CFD Target
w_i [ft/s]	-66.8	-59.7	-78.0	
D [lbs]	1575.9	1257.2	2079.6	2073.5
a [lbs]	497.6	816.3	6.1	
r [%]	24.0	39.4	0.29	
\dot{L} [lbs]	52.9	42.2	71.7	76.0
a [lbs]	23.1	33.8	4.3	
r [%]	30.4	44.5	5.6	
M [ft-lbs]	7926	5068	11310	12325
a [ft-lbs]	4399	7257	1015	
r [%]	35.7	58.9	8.2	

Validation with Integrated Co-Axial Vehicle Model for Hover and 80 Knots

The identified interference matrices for rotor interference on fuselage were incorporated into the co-axial simulation model as table lookup values. Prior to running flight dynamic analysis, the trim fuselage forces and moments were determined for several interference modeling options and flight conditions. Table 7 presents the hover comparison

between 11.77 -11.955i40(1terference)-81ter-m5[i/F10 6.0s-f3o f2wy/F10 6a6a3t1a

sengle tpint ta t.G.,-5346r-m5[i/49(tani/49(tagebraic))-349(ta20(ve15(erage)-TJ/0 -11.955 Td [(s6.0s-f3o f2wy/35(5ofy/356the))-365(5

buselage-eth bndfset

hover and 80 knots are included to show the advantages of the identified inflow model over the Peters-He inflow model.

A simplified block diagram of the co-axial vehicle control system is shown in Figure 46. Stability is maintained through the PID controller feedback of the SAS. The broken-loop response was determined by evaluating the output of the SAS, $f(s)$, for a given input

improves the accuracy of flight dynamics response and stability margins over the Peters-He model, and is thus much more suitable for FVL applications.

These findings were verified through flight dynamic analysis of the identified inflow model in comparison to VPM simulation. For the co-axial configuration considered, the identified inflow model achieved an excellent match for all controls channels at several airspeeds, supporting the conclusion that the identification methodology is the appropriate choice for multi-rotor simulation.

Acknowledgment

This research was sponsored by the US Army SBIR program under contract No. W911W6-17-C-0018 and

[20] Johnson, W.; Moddie, A. and Yeo, H., "Design and Performance of Lift-Offset Rotorcraft for Short-Haul Missions, AHS FVL Conference, SF, CA, Jan. 2012

[21] Tischler, M.B., Berger, T., Ivler, C.M., Mansur,

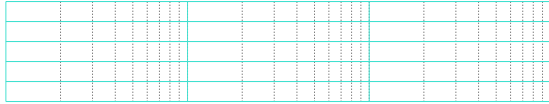


Figure 5: Upper rotor cosine inflow state ($\frac{1}{2}c1$) response to excitation of a hub pitch moment based inflow forcing function ($\frac{1}{2}c1$) at 40 knots



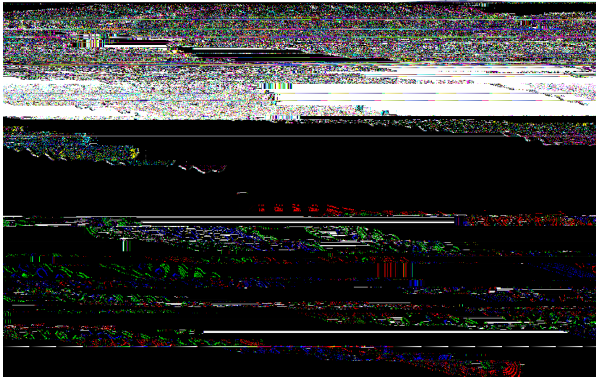


Figure 9: A snapshot of VPM rotor wake (left sideview) showing the wake distortion due to the lower rotor TPP rotation at 40 knots

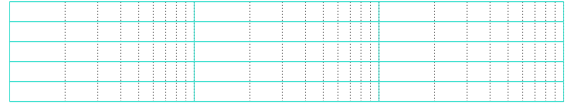


Figure 12: $\frac{1}{2}s^2=p$ transfer function fit at 40 knots

Figure 10: $\frac{1}{2}c^2=q$ transfer function fit at hover

Figure 13: Identified K_r factors as a function of airspeed

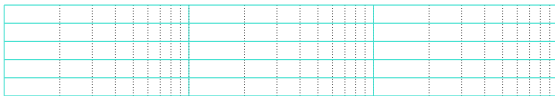


Figure 11: $\frac{1}{2}s^1=p$ transfer function fit at 15 knots

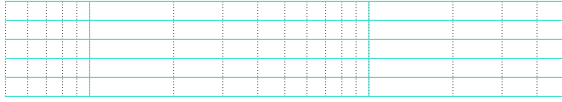


Figure 15: Co-axial nonlinear model roll rate off-axis response to a longitudinal frequency sweep at hover, $\rho=X_b$

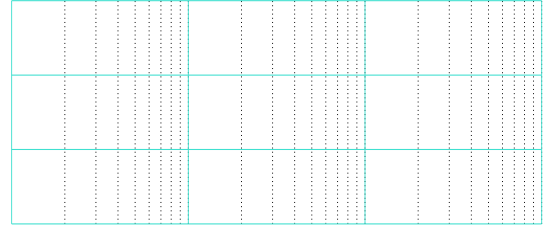


Figure 18: Nonlinear and linear flight dynamics model pitch rate frequency response with TPP rotation effect at hover, $q=X_b$

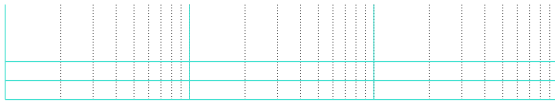


Figure 16: Co-axial nonlinear model upper rotor cosine inflow state response to a longitudinal frequency sweep at hover, $\frac{1}{2}c^1=X_b$

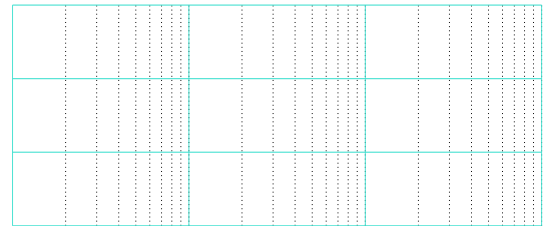


Figure 19: Nonlinear and linear flight dynamics model

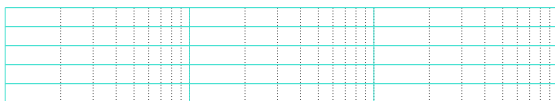


Figure 17: Co-axial nonlinear model upper rotor flapping response to a longitudinal frequency sweep at hover, $\frac{1}{1s}=X_b$

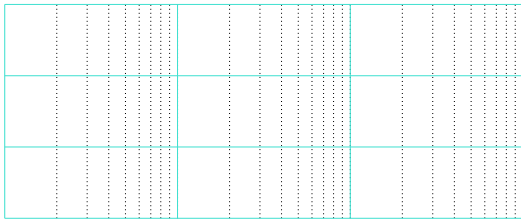


Figure 20: Linear flight dynamics model pitch rate response with and without TPP rotation effect at hover, $q=x_b$

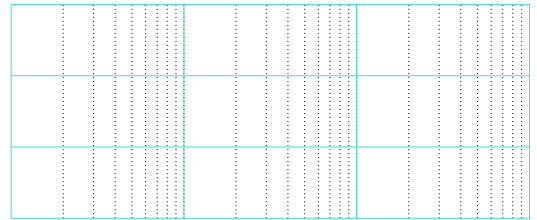


Figure 22: Linear flight dynamics model roll rate response with and without TPP rotation effect at hover, $p=x_a$

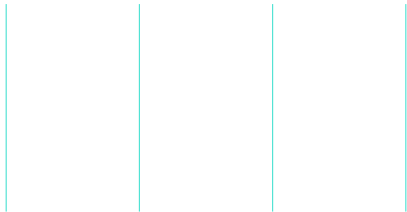


Figure 21: Linear flight dynamics model pitch rate and angle time domain response with and without TPP rotation effect at hover, $q=x_b$

Figure 23: Linear flight dynamics model time domain roll rate response with and without TPP rotation effect at hover, $p=x_a$

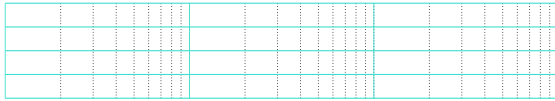


Figure 24: Co-axial nonlinear model pitch rate response to a longitudinal frequency sweep at 40 knots, $q=x_b$

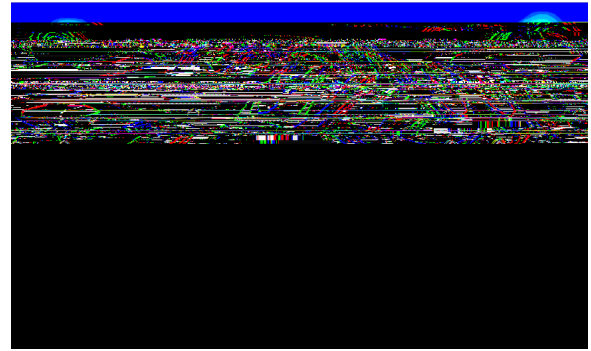


Figure 27: VPM wake X-plane slice with empennage sampling point locations, 80 knots

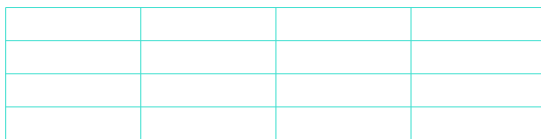


Figure 25: Co-axial nonlinear model pitch rate and angle response to a longitudinal doublet at 40 knots, $q=x_b$

Figure 28: Upper rotor interference velocity on right stabilator at 80 knots



Figure 26: VPM wake Y-plane slice with vertical fin sampling point locations, 80 knots

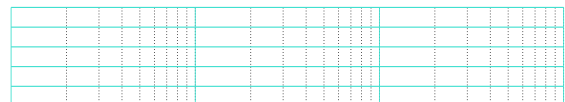


Figure 29: Gain and time delay fitting for the response of the upper rotor interference velocity on right stabilator at hover, $w_z = \begin{matrix} 0c1 \\ 1 \end{matrix}$, fitting cost = 3.7

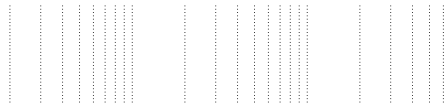


Figure 30: Co-axial vehicle pitch rate response to a longitudinal frequency sweep at hover, $q=x_b$

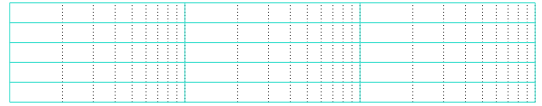


Figure 32: Co-axial vehicle heave response to a collective frequency sweep at hover, $Az_i=x_c$

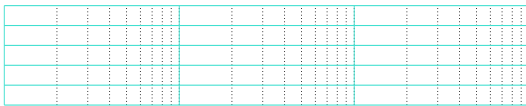


Figure 31: Co-axial vehicle roll rate response to a lateral frequency sweep at hover, $p=x_a$

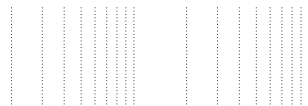


Figure 33: Co-axial vehicle yaw rate response to a pedal frequency sweep at hover, $r=x_p$

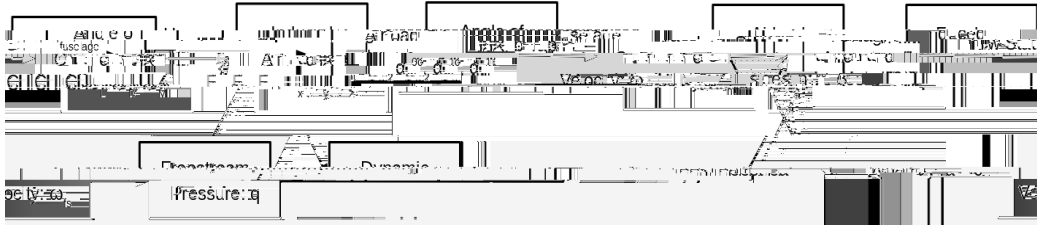


Figure 34: Data flow from rotor inflow states to fuselage forces and moments



Figure 35: Variation in rotor interference velocity with location on fuselage surface at 20 knots forward flight



Figure 36: Co-axial vehicle fuselage geometry with locations of interference sampling points

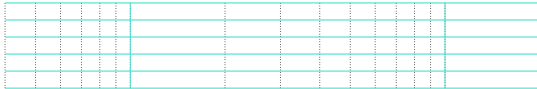


Figure 37: Example gain and time delay fitting for downwash response to upper rotor uniform inflow state, $w = \frac{0c1}{1}$ [ft/s], for the effective rotor interference velocity on the fuselage

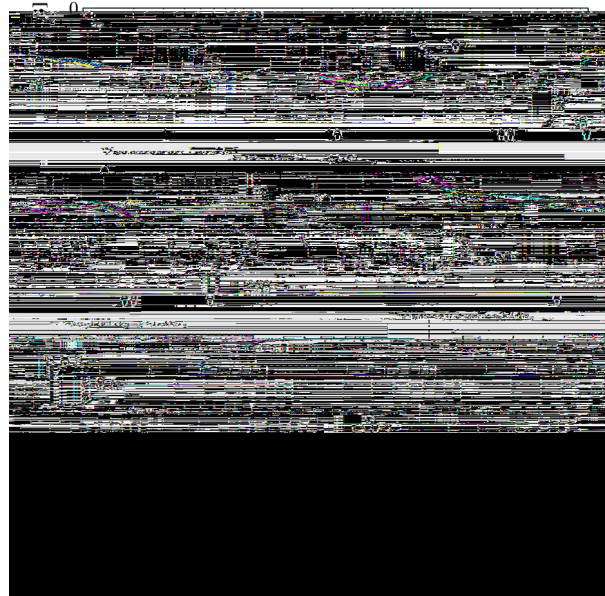


Figure 39: Co-axial vehicle roll rate response to a lateral frequency sweep at hover, $p = X_a$

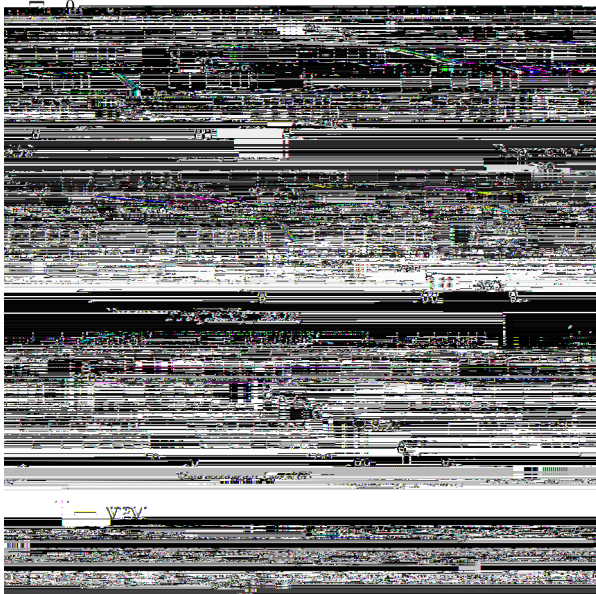


Figure 38: Co-axial vehicle pitch rate response to a longitudinal frequency sweep at hover, $q = X_b$

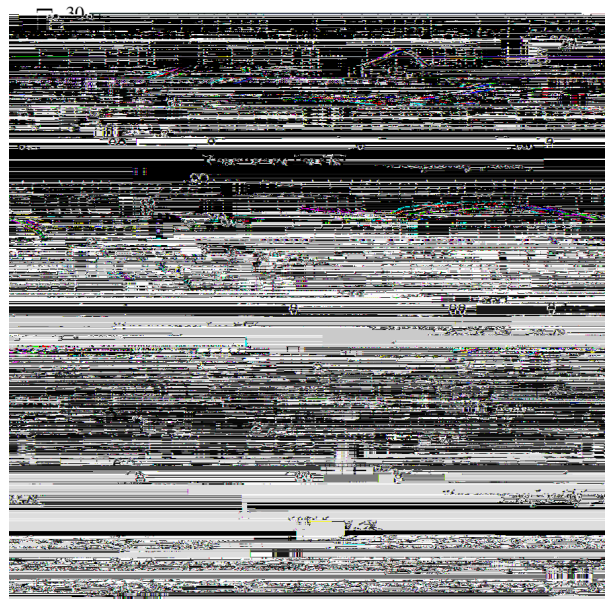


Figure 40: Co-axial vehicle heave response to a collective frequency sweep at hover, $Azi = X_c$

Figure 45: Co-axial vehicle heave response to a